UNIVERSITY OF TURKU

Processing of novel nickel free stainless steel by laser powder bed fusion additive manufacturing

Mechanical Engineering/Faculty of Technology

Master's thesis

Author(s):
Tuomas Kantonen

Supervisor(s):
Prof. Ashish Ganvir &
Dr. Sneha Goel

29.3.2023

Turku

Master's thesis

Subject: Mechanical Engineering, Additive Manufacturing
Author(s): Tuomas Kantonen
Title: Processing of novel nickel free stainless steel by laser powder bed fusion additive manufacturing
Supervisor(s): Professor Ashish Ganvir & Dr. Sneha Goel
Number of pages: 40 + 2 pages
Date: 29.3.2023

Additive manufacturing (AM), also commonly known as 3D-printing is a modern manufacturing technology for building products using computer aided design (CAD) models in a layer-by-layer fashion, thereby allowing complex geometries to be produced which might be difficult or even impossible to manufacture traditionally. One of the most widely used AM techniques, especially to build metal products, is laser powder bed fusion (L-PBF) which uses laser to melt material in powder form to create solid parts in a layer wise fashion. As it is with any manufacturing process, the L-PBF produced part quality is strongly dependent on its numerous processing parameters. Therefore, depending on L-PBF process parameters, the produced parts' characteristics such as density, surface quality, microstructure, properties, etc. can vary widely. These parameters can be related to laser, scanning strategy, powder, and both build plate and powder bed temperatures. Finding optimal building parameters can be very difficult since there are numerous variables in the L-PBF process. Making the process reliably repeatable is one of the biggest current challenges of L-PBF to reach the potential of being industrially worthy manufacturing method.

Stainless steels are widely used material group in everyday utensils and in many industrial sectors. Great part of stainless steels include nickel which can cause health hazards and is an expensive element. Due to health issues related to nickel usage, there have been efforts to reduce its utilization especially in products used for biomedical application. Research on processing nickel free steels by L-PBF is in very initial stage. Nickel free steels have many applications in various industries, especially in health technology sector. Since L-PBF has already been identified as a potential manufacturing method to support various health technology business sectors such as biomedical implants, it is worth looking at how L-PBF can be used to process medically relevant Nickel free stainless steels.

Therefore, in this study, novel stainless-steel powder with negligible Nickel content (hence Nickel free) was processed using Aconity3d MIDI+ L-PBF machine. Several different L-PBF process parameter combinations were studied to get different volume energy density (VED) to find out optimal combinations to produce dense and deformation free specimens. The study identified laser power, scanning speed and hatching distance as the key process parameters and were optimized. Moreover, the study also investigated the effect of the support structures on specimen deformation and density.

Small cuboid shaped specimens were successfully produced with multiple parameter combinations. Defects were seen in lower VED and higher VED specimens. In lower VED specimens delamination and cracking were commonly observed and in higher VED specimens over melting was significant. Four different parameter combinations yielding defect free specimens were chosen for further examinations. Although not in the scope of this study, there were specimens printed for mechanical testing with the chosen combinations for further investigation. The microstructure and phase composition of these specimens was examined in this work. In as-built condition, the austenitic phase was present in small amount, however it was significantly increased through appropriate post-process heat treatments.

Key words: Additive manufacturing, laser powder bed fusion, nickel free steels, 3D-printing

Table of contents

Acknowledgements

First and foremost, I would like to express my deepest appreciation to my supervisors Professor Ashish Ganvir and Dr. Sneha Goel for their invaluable feedback, continuous support and patience during my Master's thesis. I'm extremely grateful to the Department of Mechanical and Materials Engineering at University of Turku for funding my Master's thesis. I'm also thankful for the tenure track grant for Professor Ashish Ganvir to cover research cost as well as travel visit cost to Paul Scherrer institute (PSI). Many thanks to Dr. Efthymios Polatidis and Dr. Jan Čapek from PSI for their constant support in scientific discussion about materials science and process parameter optimization. Big thanks also to Dr. Jan Čapek for all the microscopy, density measurements and EBSD. Special thanks to Dr. Jukka Pakkanen from SME Elektro-Group Ltd. for the help with process parameter optimization. Many thanks also to Professor Antti Salminen and Dr. Heidi Piili from University of Turku for their advice during my Master's thesis. I would also like to thank the whole staff of Machine Technology Centre Ltd. for their help on practical things related to performing my Master's thesis. Lastly, I would like to extend my sincere thanks to my family. Without their tremendous patience and understanding in the past two years, it would not be possible for me to complete my study.

1 Introduction

Additive manufacturing (AM), popularly called as 3D-printing, is rising from being tool for prototyping into a new way to produce real industrial components. As it started from plastics the variety of materials possible to be processed with AM has spread from biomaterials and ceramics to various metals. While the existing materials are finding new applications through AM, new materials are also being developed solely for AM purposes. The research on the new materials is hot topic as there is ambition to create improved and new products manufactured through AM. Certain materials have already shown to have better features after processing via AM route than made traditionally. (Gibson et al. 2021.)

Laser powder bed fusion (L-PBF) also commonly known as Selective Laser Melting (SLM) is one of the most widely accepted AM method that has gained broad attraction in research in recent years, especially when it comes to manufacturing metal parts. It has benefits like possibility to produce near-net-shape complicated metal parts from wide variety of materials as well as customised microstructures. (Sofras et al. 2022.)

Steels are one of the most widely used materials for various applications, especially austenitic stainless steels have many applications in different industrial sectors and everyday life. In fact, stainless steel is among one of the most widely experimented material with L-PBF by various research groups worldwide (Akilan et al. 2022, Boes, Röttger, & Theisen 2020, Cui et al. 2019, Freitas et al. 2022, Karimi et al. 2021, Li et al. 2012, Liu et al. 2015, Merot et al. 2022, Simson et al. 2017, Sofras et al. 2022, Uddin et al. 2022). Stainless steel is an Iron based alloy consisting of several elements such as chrome, nickel, molybdenum, copper, titanium, aluminium, nitrogen and niobium, with each element playing a crucial role in determining the overall property/characteristics of the material such as corrosion resistance, mechanical strength etc. Among these various alloying elements, chromium and nickel are present in relatively higher amounts. (Davis 1994.) It is a well-known fact that nickel can cause health problems e.g., allergic reactions on skin contact. Even though the material can be considered as corrosion resistant there can still be enough nickel ions dissolved by sweat or other body fluids to irritate the skin and cause inflammation. Nickel has been used in stainless steels to stabilize the austenitic phase which provides superior ductility, formability and toughness with good corrosion resistance. But due to health issues related to nickel, there have been actions to avoid its usage. (Gavriljuk & Berns 1999.) Therefore, this need has driven attempts to develop different nickel free steels. (Davis 1994, Menzel, Kirschner &

Stein 1996.) In an attempt towards minimizing the role of Nickel in stainless steel, the present study showed for the first time 3D-printing of novel Nickel free stainless-steel using L-PBF. Experiments were made with Aconity3D MIDI+ machine to form dense and deformation free specimens from the spherical powder of Nickel free steels.

The structure of the thesis is as follows: The first two chapters cover the relevant theory on AM and L-PBF including limitations of the technology, and also about the processed material, i.e., stainless steels. The third chapter is about materials and methods used in the study. In the fourth chapter the results from the study are presented and in the fifth chapter these results are discussed together with findings from prior studies. And finally, in the sixth chapter the conclusions drawn from this thesis work are presented.

2 Theory

Additive manufacturing is debated to be one of the pillars of the next generation industrial revolution due to its potential to disrupt almost every manufacturing sector. For AM, a three-dimensional model is created in Computer Aided Design (CAD) and the CAD file is then sliced into thin 2D layers, with each layer having appropriate thickness, typically 50-90 micron and converted into a STL file which is then transferred to the AM machine. In AM machine the part is then built in a layer-by-layer fashion following the sliced CAD model. After the build is finished the part is removed and post-processed, and these steps typically include cleaning, support structure removal and thermal treatment. A key advantage of AM compared to traditional manufacturing is its ability to produce complex parts especially with shorter lead times. Traditionally, parts are produced by subtractive way, that is by removing the material from a bigger part, which needs careful planning and more importantly causes huge material wastage. Furthermore, AM gives possibilities to process new materials for manufacturing. Some materials are in fact customized (in terms of shape, size distribution etc.) only for AM. (Gibson et al. 2021.)

Additive manufacturing is the next generation technology that is considered to play a significant role in transitioning towards sustainable manufacturing. The part design can be done in one centred location and then digitally delivered all around the world to factories. In these factories parts can be produced using AM technologies as and when needed, thereby saving expenses and time related to inventorying management and shipping. AM causes significantly less material waste since material is deposited in appropriate amount at needed place. Using energy resource like nonpollution laser during AM, this is considered to be even more sustainable. (DebRoy et al. 2018, Gu 2015.)

2.1 AM technologies

The American Society for Testing and Materials (ASTM) group “ASTM F42 – Additive Manufacturing” classified the several different AM techniques in seven categories. Process using selectively delivered energy to solidify certain area on liquid photopolymer is called Vat Photopolymerization (VPP). Powder Bed Fusion (PBF) processes include techniques where powder bed is selectively processed with energy sources like laser or electron beam. In Material Extrusions (MEX) substance is extruded through a tip. Material Jetting (MJT) means placing beads of material selectively. Processes where liquid adhesive is deposited to powder

bed are Binder Jetting (BJT). In Sheet Lamination (SHL) sheets of substance are joined to form a part. And finally processes involving simultaneous melting (material in powder/wire form) and deposition of the material on a surface are called Directed Energy Deposition (DED). When it comes to metal AM, PBF and DED using powder are most common. (Gibson et al. 2021.)

PBF is one of the most attracting AM method, especially, when it comes to metal AM processes. The metal PBF processes using laser energy (L-PBF) have been more in the focus for development than the ones using electron beam. (Gibson et al. 2021, Gu 2015, Sames et al. 2016.) Among other factors, this could be particularly attributed to the versatility of the technique to enable processing of relatively wide range of materials. During PBF, powder particles are heated by absorbed photons from laser beam in L-PBF and by kinetic energy from electrons in electron beam PBF (EB-PBF). Limitation with EB-PBF is the negative charge the powder gets from electrons which causes repulsive force between negatively charged particles which can lead to burst causing “powder cloud”. As a result, the powder particles can fly around in the machine and jeopardize the processing. For example, the particles can interact with the electron beam and cause undesired scattering of the beam reducing its efficiency. (Gibson et al. 2021.)

In DED, the energy source is used to create a melt pool on the substrate and simultaneously material is introduced into the melt pool using external mechanical device called as feeder. The energy source is typically mounted on an industrial robot and the substrate is typically fixed to a mechanical rotating or stationary fixture. A desired amount of material is then deposited layer-by-layer to build a 3D part. The material can be in powder or wire form. DED is especially suitable for repairing and building on existing parts and it is drawing interest in industry based on its capability to form near-net-shape products faster and cheaper than traditionally manufactured near-net-shape products. (Gibson et al. 2021.)

2.2 Laser Powder Bed Fusion

In L-PBF, desired amount of powder equivalent to the layer thickness of the 2D sliced layer of the 3D part is spread on a building platform. Then the area based on CAD file is scanned with laser which selectively melts the powder to a depth that exceeds the layer thickness so that the previously solidified structure is partially re-melted, and layers are bonded well creating high density parts. The process repeats layer-by-layer until the desired part thickness is reached and the complete part is printed. (Gibson et al. 2021.)

Basically, any material that can be hardened after melting can be used in L-PBF processes. So, polymers, composites, metals, ceramics and ceramic composites are all possible materials for powder bed fusion. But as mentioned before powder bed fusion is mostly raising interest in AM of metals, so many different metal powders have been used in PBF processes. Steels and several steel alloys, titanium, nickel-based alloys, aluminium alloys, cobalt-chrome and even silver and gold are available for PBF. (Gibson et al. 2021.)

2.2.1 L-PBF process parameters

In L-PBF, process parameters can be categorized into four groups. Laser based parameters such as laser power, and spot size; scanning parameters such as scan speed, hatch or line spacing and scan pattern; powder parameters such as particle shape and size, layer thickness and material properties; and finally heat parameters such as powder bed temperature and build plate temperature. (Gibson et al. 2021.)

The laser melts powder to a certain depth and width depending on the varied process parameters as mentioned above. For example, the size of the melt pool which is considered as one of the most crucial factors to control the quality of the printed part is strongly dependent on key parameters such as laser power, scanning speed, spot size, build plate temperature and powder bed temperature (Bertoli et al. 2017, Yang et al. 2022). For the same laser power and other parameters, lower scanning speed gives higher energy to the area causing deeper and wider melt pool. To get sufficient fusion between the layers the melt pool needs to extend to previous layer, that is beyond the typical layer thicknesses used in L-PBF which are from 0.02 to 0.15 mm. Scan spacing also called hatch distance determines the melt pool overlapping between the scans. Melt pool overlapping affects mechanical properties of the printed parts. Shape and size of the powder as well as the spreading of the powder can affect the quality of the part. Density of the powder bed depends also on the shape or morphology of the powder. Higher powder bed density gives higher thermal conductivity to the powder bed which creates better mechanical properties for the produced part. (Gibson et al. 2021.)

2.2.2 Limitations of L-PBF

The very complex nature of L-PBF process due to several factors, predominately the numerous process parameters and their interdependence can create several issues during printing leading to difficulties in producing desired high-quality parts. Even though there are many different L-PBF systems available in the market, with their own assets and constraints

there is still doubts how well PBF metal AM is primed for industrial manufacturing (Moshiri et al. 2019).

As said before, varied parameters in L-PBF can have a strong influence on different printed part features. The parameters and conditions in the process regulate the energy density and the result of the part quality. Higher energy density can create residual stress leading to warping and cracking but also vaporization causing pore formation to the part. (Simson et al. 2017.) On the other hand, lower energy density can cause poor flowability and small connection region which leads to balling phenomenon and increased surface roughness (Li et al. 2012). Usually, giving high laser power on high powder bed temperature gives dense products but there can be troubles of cleaning the products as well as recycling the powder. On the other hand, using low laser power and low powder bed temperature gives more precise products with lower density and possibility of layer delamination. Using high laser power and low powder bed temperature may lead to uneven shrinkage and accumulation of residual stresses which leads to warping. (Gibson et al. 2021.) The building up of residual stresses is a result of fast cooling and subsequent solidification shrinkage and thermal contraction. Besides residual stresses it is more likely to create microstructures that are not desired. (Narasimharaju et al. 2022.)

There are two mechanisms in L-PBF that can result in increased residual stress, a) a temperature gradient mechanism (TGM) and b) the cooling stage of the top layers. In TGM, a high temperature gradient is generated by the quick heating of the top layer by the laser beam and considerably slow heat conduction. Compressive stress is created when expansion of the hot surface is limited by the layers below. Once material's yield strength is attained the surface layer will be plastically compressed. Since there are no mechanical constraints the parts bend away from the laser beam. While cooling, the top layers shrink and start to bend towards the laser beam. The second mechanism causing residual stress is due to shrinking of the top layer because of thermal contraction, which is again restricted by the layers below. This will cause tensile stress to top layers and compressive stress to the lower layers. (Mercelis & Kruth 2006.)

The residual stresses accumulate causing macroscopic cracks in the product usually at or around geometrically sharp locations like the edges of the part or the interface between the build platform and the build material. Cracking usually happens in regular distance because of the accumulation of the stresses formed in L-PBF process. (Platl et al. 2022.) Extreme case of

cracking is once the residual stress exceeds the yield strength of the material which leads to the complete separation of two adjacent layers from each other which is also called as delamination. (Mukherjee, Zhang & DebRoy 2017.) Delamination can also be a consequence of flaws in powder recoating which may lead to inferior fusion of two adjacent layers (Colosimo & Grasso 2020).

The microscopic cracking is dependent on the volumetric energy density and scanning strategy of L-PBF technology since those affect the columnar crystal size and growth orientation. The cracks formation is eased when coarse columnar crystals and straight grain boundaries are formed. (Li et al. 2023.)

Another challenge in L-PBF is formation of porosity in the printed parts. Different types of porosity are formed in L-PBF printed parts such as keyhole porosity, lack-off of fusion porosity and gas porosity. Keyhole porosity is partially related to the deep and narrow melt pool. Keyholes appear under conditions where laser power is high and scanning speed is low. Pores near the end of the keyhole are moved away from the keyhole and get closed to be flaws in the part. This happens in critical keyhole instability which creates acoustic waves in the melt pool providing driving force for the pores. (King et al. 2014, Zhao et al. 2020.) Lack-of-fusion porosity is generated when melt pool penetration depth is not sufficient and overlapping of subsequent melt pools are too far from each other and some of the powder is left unmelted between them (Reijonen et al. 2020, Tang, Pistorius & Beuth 2017). Gas porosity occurs due to previous gas pores from the atomization production process of the powder. It can also happen if shielding gas or vaporizing alloys in powder get entrapped in melt pool. (DebRoy et al. 2018, du Plessis 2019.) Also, the effectivity of the inert gas flow in clearing the by-products from the impact zone of the laser on the powder bed affects vigorously the melt pool. That is some of the laser energy is absorbed by the by-products and less energy than intended is absorbed to the powder bed. Inefficient clearance of the by-products might also cause higher porosity of the actual products. (Boes, Röttger & Theisen 2020, Wang et al. 2017.) Even the type of inert gas, e.g., if it is argon or nitrogen might make a difference in this, since they have different densities which will cause different gas flow characteristics and therefore the absorbed energy in the powder bed may vary (Boes, Röttger, & Theisen 2020).

Another challenge in L-PBF is also the formation of spatter. Spatter is created either by the tearing of the molten metal, called as droplet spatter or when non-melted metal powder

particles around the melt pool are blown away, called as powder spatter. They both cause metallic vapor above the impact zone, once the laser beam is absorbed small metal particles are formed. If the spatters are not removed by inert gas flow and they fall on the powder bed they can be re-melted by laser leading to undesired final product properties such as density, microstructure and mechanical properties. Since L-PBF include several complicated phenomena containing quick melting and solidifying of the powder but also dynamics and heat transfer of the melt pool and so spattering is influenced by various components, therefore it is very difficult to predict spatter behaviour. But usually, spattering is more intense when the energy load is higher. On average the spattering particles are clearly bigger than the original powder size leading to uneven powder distribution which is harmful to laser to make consistent and uniform melt tracks. (Liu et al. 2015, Wang et al. 2017.)

2.3 Stainless steels

Stainless steels are iron based alloys containing at least 11% of chromium which inhibits rusting in uncontaminated environment. There are various other elements combined to achieve better properties e.g., nickel, molybdenum, nitrogen, and carbon. Usually, carbon content is from less than 0.3% to over 1.0%. Stainless steels are presented in four groups based on their microstructure: ferritic stainless steel which has body-centred-cubic (BCC) structure, austenitic stainless steel which has face-centred-cubic (FCC) structure, martensitic stainless steel which has body-centred tetragonal (BCT) structure and duplex stainless steel which includes both BCC and FCC structure in similar proportion. Among all, austenitic stainless steel is the most used group. There are two categories of austenitic stainless steels: chromium-nickel and chromium-manganese-nitrogen alloys. The second category has often low nickel and high nitrogen level. Nitrogen substitutes nickel as an austenite stabilizer and manganese is needed to enhance solubility of nitrogen but also inhibiting transformation to martensite. (Davis 1994.)

Austenitic steels that contain nickel have excellent properties like superior ductility and corrosion resistance and are commonly used in various industries, especially in medical applications and everyday items. Downside in using nickel is its consequences on human health. Most common health problem that nickel can cause is allergic reactions with skin, but also more severe carcinogenic relations on accumulation of nickel in the body has been reported. (Yang & Ren 2010.) Use of nickel containing alloys in prosthetics is based on good resistance against surface corrosion but still they are influenced by corrosions like pitting,

crevice, and stress corrosion. This causes of course a big risk of dissolving of nickel ions to human body but also possibility to prosthetic to crack. Changing prosthetic manufacturing to other materials such as titanium or cobalt is problematic since those are very expensive and those alloys also include nickel. To reduce use of materials that contain nickel in health or biomedical applications there has been legislations in Europe and USA. (Menzel, Kirschner & Stein 1996.)

There are only limited number of iron-based materials that can be used to produce dense parts by L-PBF. Different elements in the iron-alloy have different effects on multiple physical phenomena that are present in the process of PBF. These phenomena are for example heat transfer, laser absorption, and spreading of the melt etc. (Rombouts et al. 2006.) The chemical composition can also affect the phase composition of steels built AM, depending also on the technique and parameters on the process. Traditionally manufactured steels usually have only single-phase structure whereas AM steels may have single- and multiphase structures. Compared to fully austenite steels having ferrite or other phases the properties can vary remarkably, e.g., strength could rise and ductility and corrosion resistance could reduce if dual phase steels are produced. (Astafurov & Astafurova 2021.)

2.4 Nickel free steels

Nickel free ferritic and martensitic stainless steels might not be tough enough for many applications. Also nickel free martensitic stainless steel does not have corrosion resistance which is required in most applications. For stainless steel to be austenitic and nickel free there needs to be adequate amounts of nitrogen, carbon, cobalt and manganese. (Speidel, Magdowski, & Uggewitzer 1996.)

Nitrogen has the same ability to stabilize austenitic structure as nickel, but also ability to make the steel more resistant to corrosion and it also strengthens the austenite steel. For this reason, there have been attempts to produce austenitic stainless steels with increased nitrogen and molybdenum contents and lowered carbon and nickel for use i.e., in chemical industry and medical applications. (Stein & Hucklenbroich 2004, Yang & Ren 2010.) High nitrogen steels (HNS) have up to 0.9 mass% of nitrogen in solid state. In high nitrogen containing steel powders used in laser AM the nitrogen content should be lower than in traditional HNS because there is a risk of generating gas pores and chromium nitride in the powder itself but also in the manufactured structures. (Cui et al. 2019.)

2.4.1 Previous studies on L-PBF

Table 1 shows amount of research papers between 2019 to 2022 searched from Science Direct with search words “LPBF and Ni-alloys/Ti-alloys/Steel alloys/Ni-free steels”. Nickel free steels are clearly least studied subject when related to L-PBF. Nickel free steels are studied less than half of the number of Nickel-alloys and less than third of the amount of Steel alloys in same content with L-PBF. This shows a clear lack of global research and development efforts in studying these Nickel free steels which highlights the importance of this thesis as it not only attempted Nickle free steels but took it one step further to find out how one of the most versatile metal 3D-printing technique, i.e., L-PBF can be used to produced parts from these steels.

Table 1 Research papers during 2019-2022 on L-PBF of respective alloys; in Science Direct.

	Ni-alloys	Ti-alloys	Steel alloys	Ni-free steels
Papers	857	1092	1277	418

2.5 Aim of the study

The aim of this study was to optimize the L-PBF process for creating deformation free and dense novel nickel free stainless steels. The overall objective was achieved by answering the following two research questions:

1. How to tailor the process parameters for the Aconity3d MIDI+ printer to create deformation free and dense novel nickel free stainless steels specimens?

2. What is the optimal support strategy to create deformation free and dense novel nickel free stainless steels specimens?

In Figure 1, the architecture of the study is shown. Firstly, Aconity’s own process parameter database for commonly used materials was explored as starting process parameters. Moreover, previous studies from literature on similar powders (e.g., HNS 1.4452 / P2000 (Arabi-Hashemi et al. 2020), X40MnCrMoN19-18-1 (Boes, Röttger & Theisen 2020) & X36CrMoWVTi-10-3-2 (Großwendt et al. 2021.)) printed in L-PBF process was explored to identify starting process parameters. Based on those baseline parameters, an experimental matrix consisting of different parameter combinations was made and subsequently a print plan was made, including the specimen geometry and positioning planning. With proper file the print was made and the results were examined. Based on the visual examinations the best

combinations of parameters were chosen and the print was planned again, but this time by also considering the geometry along with the positioning. This experimental printing parameter development procedure was repeated along with the evaluation of the printed specimens until optimal parameters were found which could result in creating deformation free and dense novel Nickel free stainless steels specimens. The printed specimens made out from the optimal process parameters were also examined to study their microstructure and phase composition using microscopy and X-rays. The details about experimental procedure for microscopy, EBSD and phase analysis can be found in earlier work (Čapek et al. 2022).

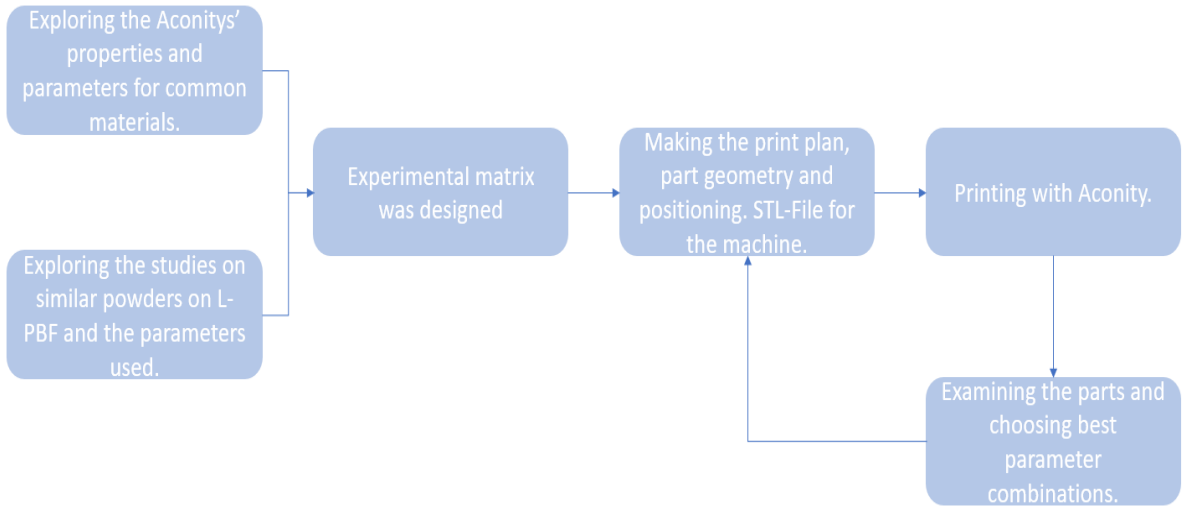

Figure 1 Architecture of the study

3 Materials and Methods

3.1 Powder

Powder used was commercially available PANACEA powder from Sandvik AB, Sweden, which is also known as a ferritic stainless-steel powder. The chemical composition of the powder is shown in Table 2. Particle size of the powder as per the supplier was d10 16.7 µm, d50 27.5 µm and, d90 48.0 µm. The dx value means diameter of particles at x% in the cumulative distribution (Arabi-Hashemi et al. 2020). Tap density of the powder as provided by the supplier was 4.8 g/cm3 and relative density 7.75.

Table 2 The chemical composition of the PANACEA powder, w-%.

Cr	Mn	Mo	Si	N	C	Co	S	P	Ni	O	Nb
17.30	11.40	3.24	0.7	0.177	0.028	0.01	0.005	0.017	0.100	0.156	0.01

Fe
balance

3.2 Aconity MIDI+

Aconity3d is a German company that manufactures LPBF machines. It was founded in 2014 and is a fast-growing company with many partnerships worldwide. Aconity MIDI+ is a laser powder bed fusion machine manufactured by Aconity3d. (Aconity3d 2022). It has numerous possible variations for technical specifications. In this study the setup used was IPG single mode ytterbium fiber laser, a spot size of 80 µm up to 500 µm, with maximum output power of 400 W and a wavelength of 1070 nm, 250 mm diameter build plate and Argon shielding gas. Picture 1 shows the setup in the laboratory environment.

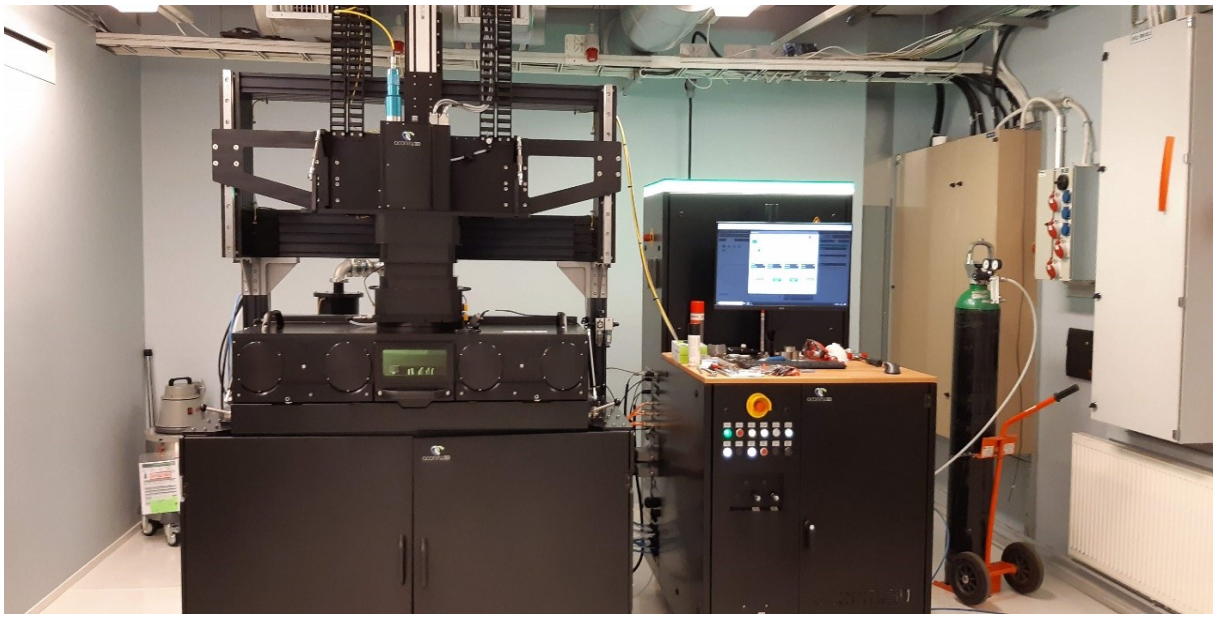

Picture 1 Aconity MIDI+ in the laboratory. Picture: Tuomas Kantonen

3.3 Parameters for MIDI+

As mentioned previously there are four groups of parameters in L-PBF process. Since the PANACEA stainless steel studied in this thesis had never been used in AM processes before, there were no known parameters to use. The powder related parameters were constant since we used the same powder during all the experimental trials for process parameter development. Furthermore, the powder bed layer thickness (d) was also kept the same throughout all the experiments, which was 30 µm since the d50 of the powder was 27.5 µm. Moreover, the parameters related to the temperature were constant since there was no preheating of the building platform nor the powder feeder in use in the current setup. So, the parameters that were varied in this study were laser and scan related. The laser power (P) used was from 110 W to 300 W, the scanning velocity (v) was from 400 mm/s to 2000 mm/s and hatch distance (h) was from 0.05 mm to 0.08 mm. Based on these values, the volumetric energy density (VED) can be calculated using equation $VED = \frac{P}{vhd}$ which gave VEDs from 46.7 J/mm^3 to 312.5 J/mm^3 (Arabi-Hashemi et al. 2020). The whole list of different combinations of the laser power, scanning speed and hatching distance created 60 different VEDs which were used to manufacture specimens (5 mm * 5 mm * 10 mm) with Aconity3d MIDI+ printer. All combinations of different parameters are shown in Appendix 1, Table 5. Reference for the parameters that were chosen based on the study of Arabi-Hashemi et al. from 2020 where similar HNS was also manufactured using L-PBF and also the Aconity's parameters for AISI 316L. The argon atmosphere with oxygen level below 2000 ppm was

kept during the experiments. The laser spot size was kept in 80 µm. Hatching strategy was hatch filling and the hatching direction was rotated by 70° with each layer. Changing the direction of the laser layer-by-layer ensues uniform heat distribution which will cause more coherent microstructure of the build part (Čapek et al. 2022).

Based on our previous printing experience with Aconity MIDI+, the contour was left out and only the hatch pattern was scanned to avoid any sharp edges formation and any additional issues. Basically, in the contour mode the shape of the sample is scanned for precision and texture matters (Gibson et al. 2021). Since precision or texture did not have any particular significance in this study, leaving out the contour mode was justified.

4 Results

4.1 The first build attempt

The first building attempt was to print 5 mm * 5 mm * 10 mm size cuboidal specimens, with 60 different parameter combinations (Appendix 1, Table 5) on the building platform, having each cuboid a different process parameter combination. The support structure used in this build is presented in the Picture 2. The support structure was chosen such that it can be easily removed from the specimens and specimens were easy to remove from build platform, as well as based on our previous experience on Aconity MIDI+.

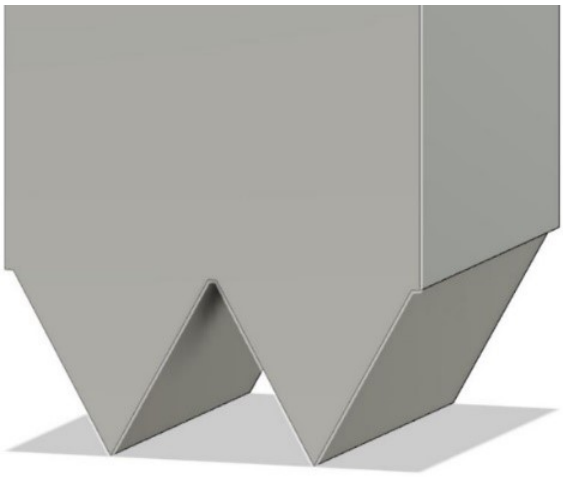

Picture 2 Design of the support structure used in this study. Picture: Tuomas Kantonen

In the first building attempt the specimens with the lower VED, parameter combination 1 to 21 (Appendix 1, Table 5), were not attached to the platform with support structure and thus these loose specimens in the powder bed were creating serious issues and disturbing the printing process. Also, some very high VED specimens were showing over melting during the visual inspection while printing. During these wide screening parameters, however, we found some process parameters in the mid-VED region and some higher VED region which could be further used to print specimens. The specimens printed using mid-VED process parameters (parameter combinations 24 to 42 [Appendix 1, Table 5]) were only built up to 5 mm height whereas using high-VED process parameters (Parameter combinations 52-60 [Appendix 1, Table 5]) specimens were built up to full 10 mm height. Picture 3 shows the building platform, the increase in VED from the left to the right and from the front to the back of the picture. Figure 2 presents the layout of the first build attempt.

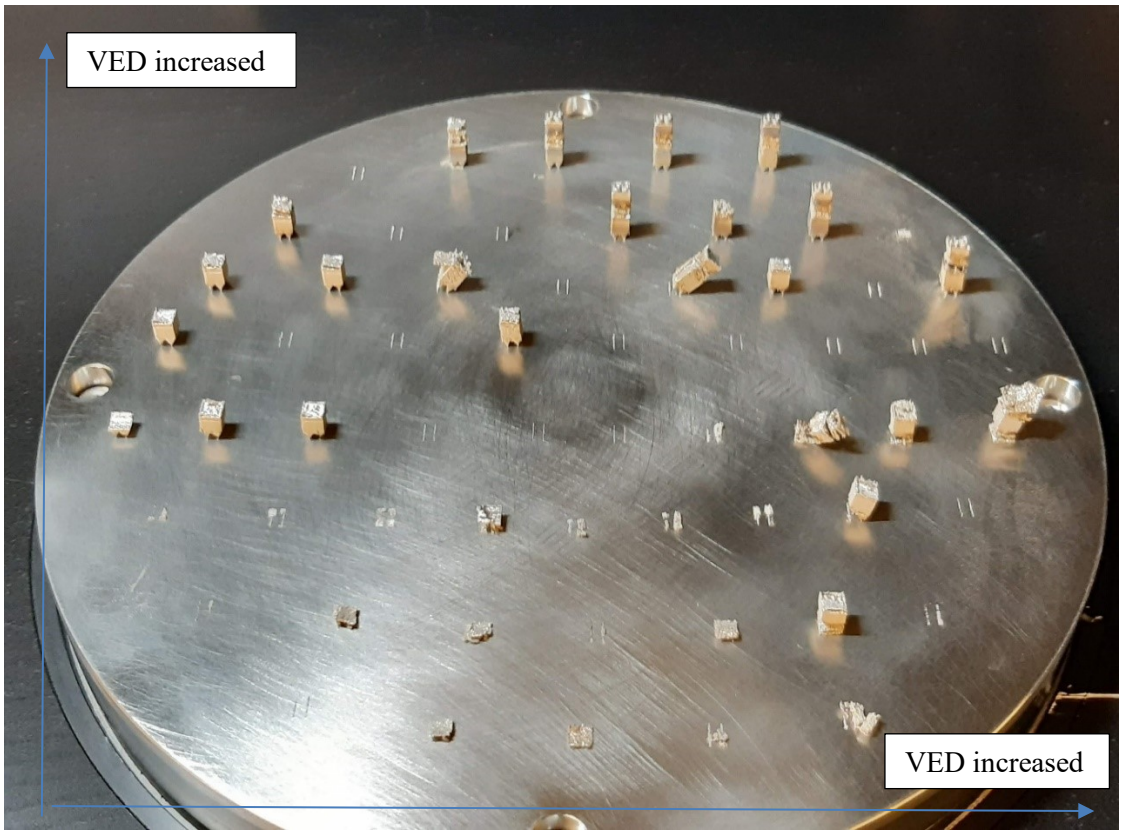

Picture 3 The result of the first build attempt. Picture: Tuomas Kantonen

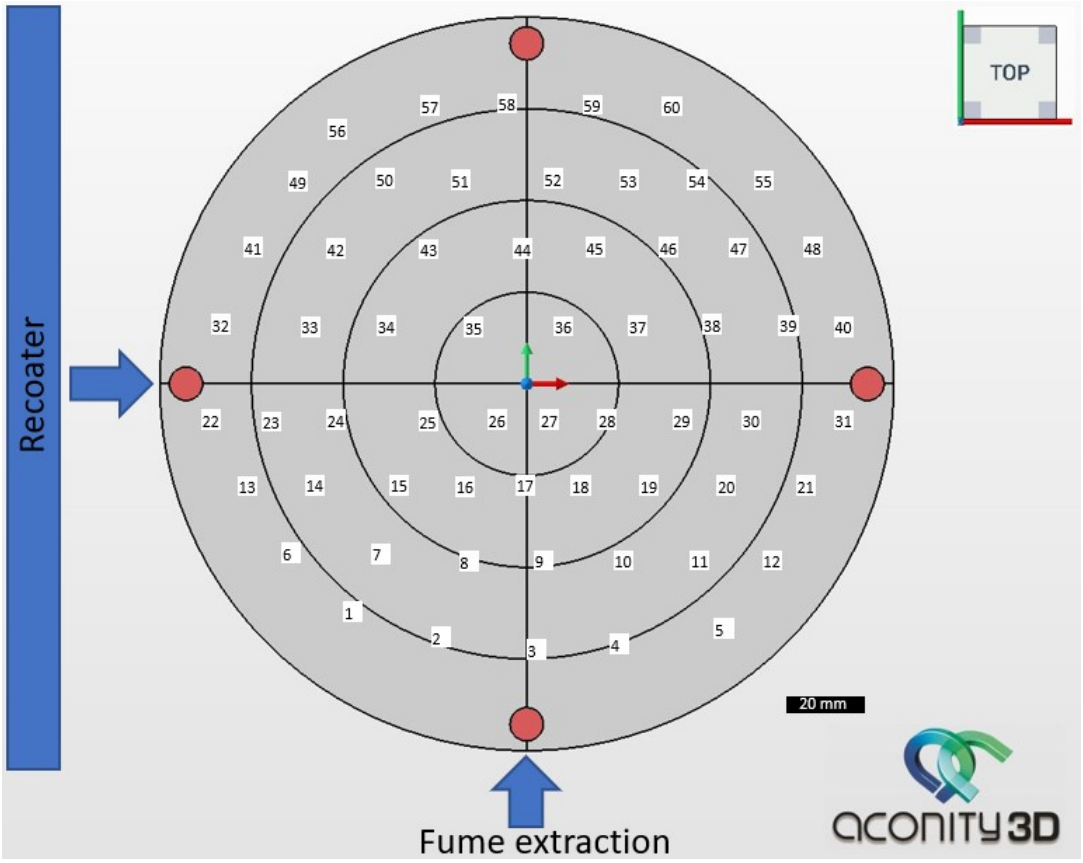

Figure 2 First build layout.

4.2 The second build attempt

Based on the learnings from the first build printing, a second build was planned. In the second build attempt, the lower VED specimens (parameter combinations 1 to 23 [Appendix 1, Table 5]) were left out and only the specimens with parameters from 24 to 60 were printed (Appendix 1, Table 5). Also, the height of all the specimens was lowered to 5 mm, so the specimens' geometry was 5 mm * 5 mm * 5 mm. The height reduction was made simply to reduce the process time since such height of the build was enough for parameter screening. The support structure was kept the same as in the first build attempt. In Picture 4, it can be seen how all the specimens in second attempt were successfully printed. However, even in this attempt, the lower VED specimens (parameter combinations 24-29 [Appendix 1, Table 5]) were barely attached to the platform.

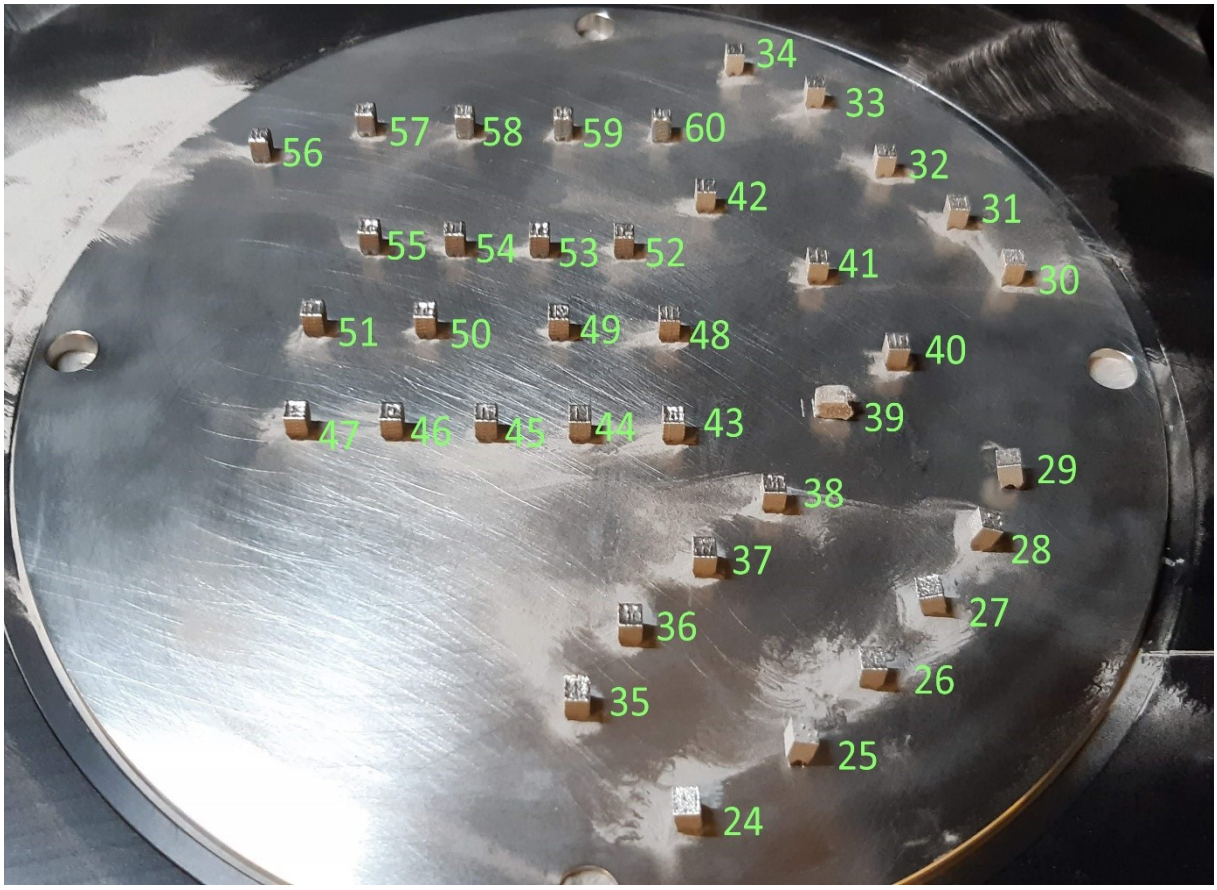

Picture 4 The result of the second build attempt. Picture: Tuomas Kantonen

4.3 The third build attempt

The third building attempt was made with low VEDs 1-23 to be built straight on the platform without any supports. Moreover, the specimen size was also changed to 10 mm * 10 mm * 5

mm. Both the no-use if support as well as the enlargement was done to see if it would make any difference to the printing of these low VED specimens without them getting detached from the build plate. In addition to low VED specimens, there were also some of the higher VED specimens with the previous support structure included in this printing attempt. Numbers printed on the specimens were also much easier to recognize since the specimens were larger. In Picture 5, it can be seen that all specimens except one higher VED specimen were again printed successfully. The one that failed was partially off from the building platform and it was aborted early to avoid any problems with continuing the printing. The reason for the failure was partially disconnected support which led to bending of the specimen.

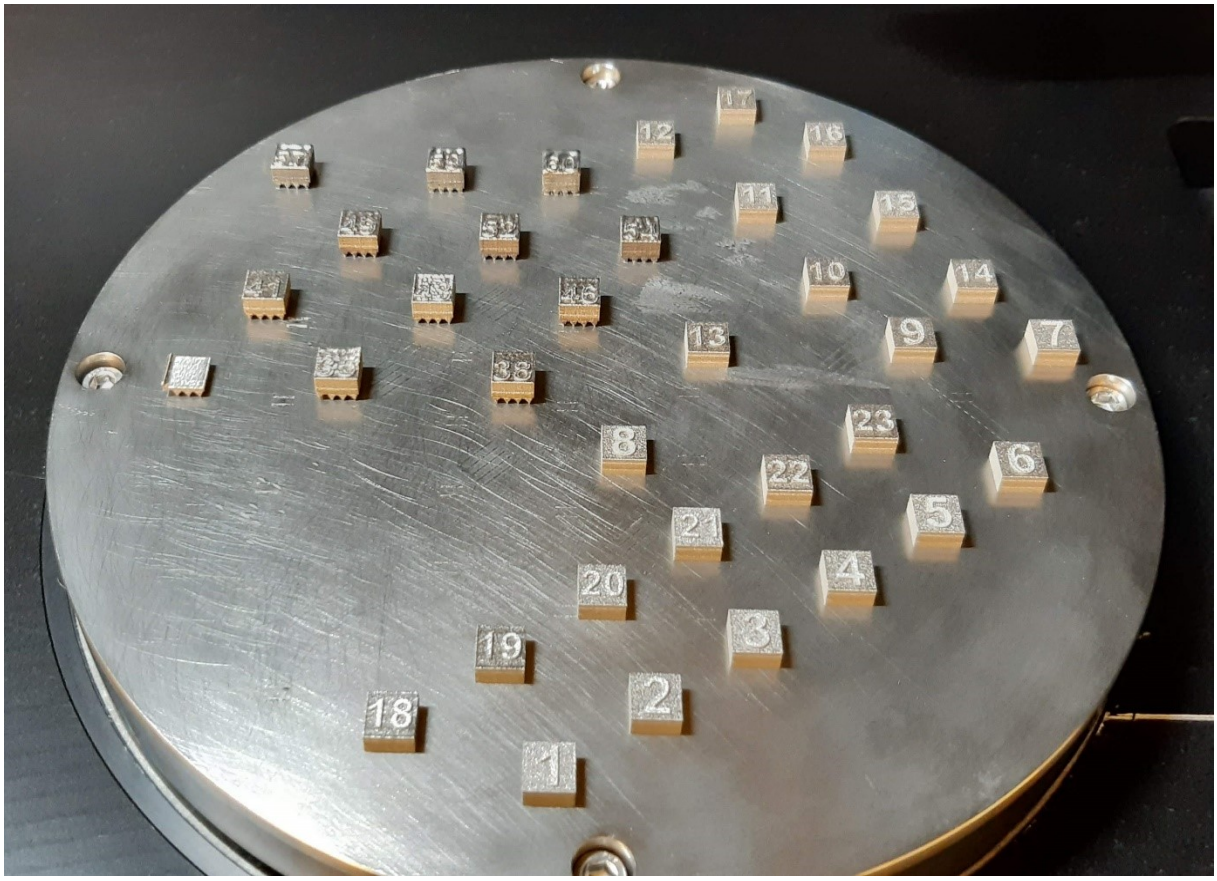

Picture 5 The result of the third build attempt. Picture: Tuomas Kantonen

Despite of successful printing, careful visual inspection showed considerably visible cracking as well as delamination in some of the specimens. Picture 6 and Picture 7 show such cracks and delamination in low VED specimens that were built straight on the building platform on the third build attempt.

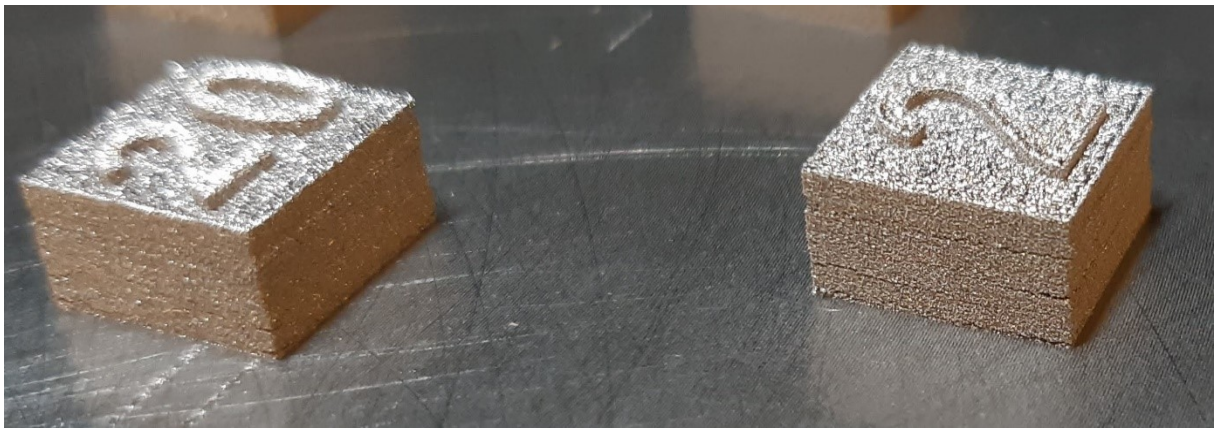

Picture 6 Delamination and cracking in the low VED specimens. Picture: Tuomas Kantonen

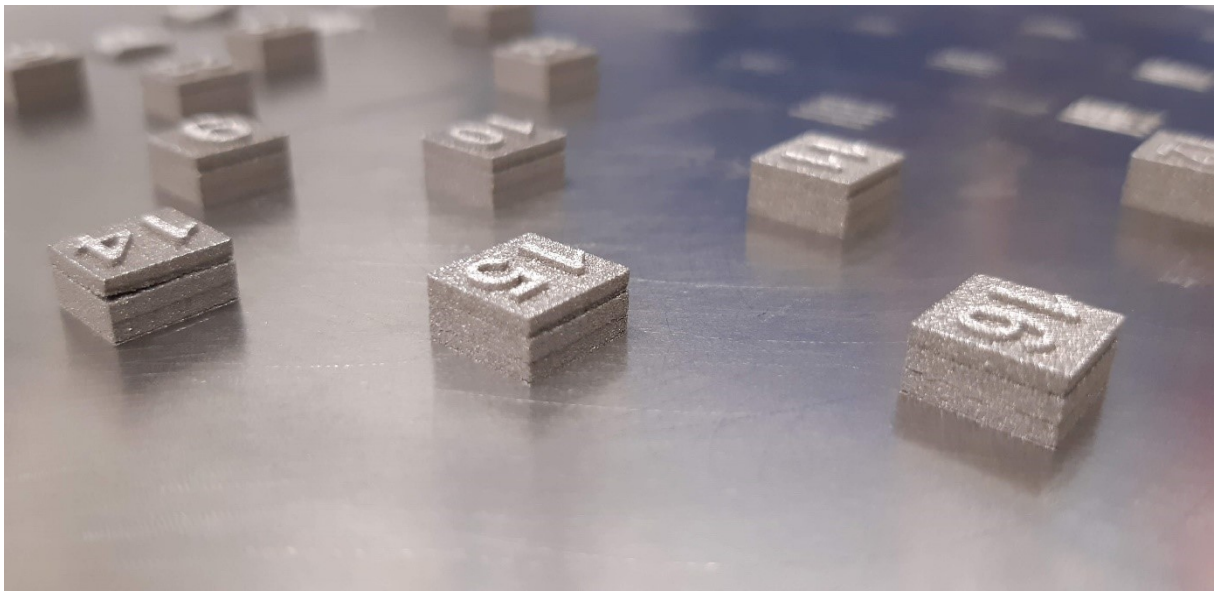

Picture 7 Delamination and cracking in the low VED specimens. Picture: Tuomas Kantonen

On the contrary, in the same third building attempt, there was clearly over melting in the high VED specimens that is seen in Picture 8.

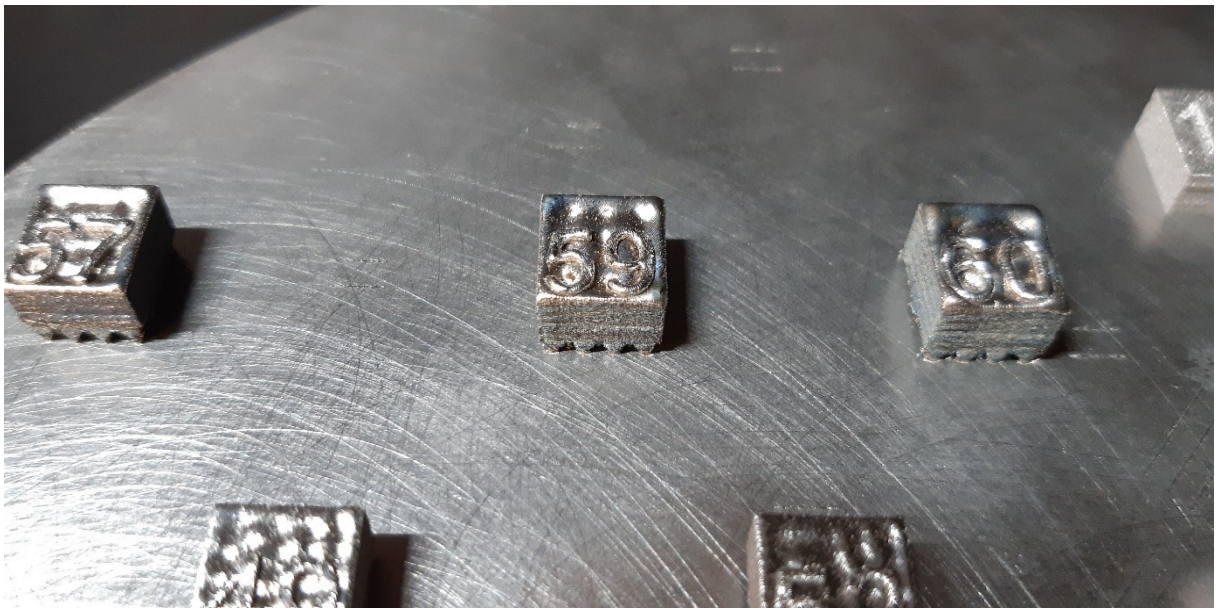

Picture 8 Over melted high VED specimens. Picture: Tuomas Kantonen

4.4 Further experiments

Based on the first three building attempts, four optimal parameter combinations were chosen for further experiments. Parameter combination number 19, 29, 42 and 60 were chosen (Appendix 1, Table 5) and 3 replicates were printed for each condition with previously used supports (see Picture 2). Based on visual observation all the specimens looked deformation and defect free. In fact, for all the specimens, the densities in as built condition were measured to be over 98% as shown in Table 3. Density measurements were made using Archimedes' principle. Accordingly, specimens were weighted in air and in water (m_2) in room temperature and densities were calculated as follows: $\rho = m_1 * \frac{\rho_{water}}{m_1 - m_2}$. Where m_1 is mass of the specimen in air and m_2 is mass of the specimen in water and ρ_{water} is the density of water. (Bai et al. 2019.)

Table 3 Specimen densities g/cm^3.

	Specimen1	Specimen2	Specimen3	Average	Density%
Parameters 19	7.620	7.604	7.582	7.602±0.019	98.090
Parameters 29	7.632	7.638	7.641	7.637±0.005	98.542
Parameters 42	7.621	7.637	7.636	7.631±0.009	98.469
Parameters 60	7.592	7.611	7.590	7.598±0.012	98.034

4.4.1 Building tensile test specimen

Next attempt with the above selected four parameters was to build longer 10 mm * 10 mm * 61 mm specimens for tensile testing. The support structures were kept as previous and the specimens were horizontally positioned on the building platform. However, the build was not successful and there were problems during the printing which was an overnight print. There was no successfully build specimen from this attempt as can be seen in Picture 9.

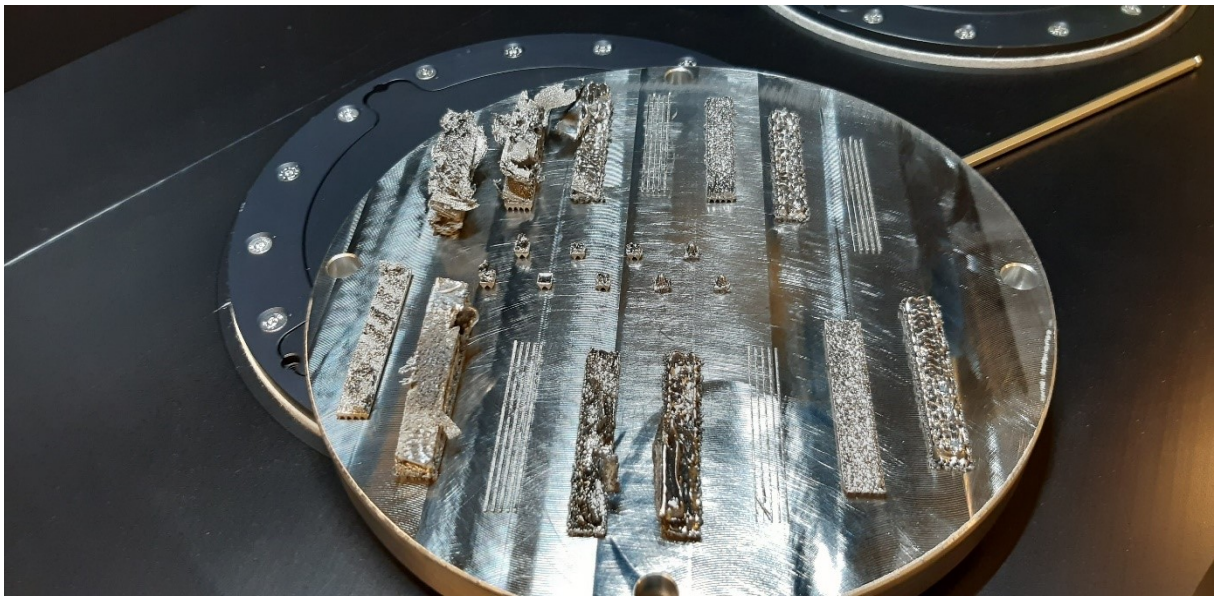

Picture 9 Build attempt for tensile specimen. Picture: Tuomas Kantonen

Therefore, we have decided to build vertical specimens using the same parameters. However, this time we have reduced the build height. Smaller tensile test specimens of size 6.5 mm * 6.5 mm * 42 mm were attempted to build vertically with the same support structures as used for building the small specimens in first trial. In this attempt there were parameter combinations 19, 29, 42 and 60 and ten replicates of each condition. However, not all the replicates were successful. Parameter 60 resulted in all 10 replicates whereas for 42, 29 and 19 there were three, two and one, respectively were successfully build which is shown in Picture 10. It was noted that the low VED parameter 19 and 29 resulted in the worst attachment of the specimens to the build platform. Even the mid VED parameter 42 showed poor attachment of the specimens with the build platform. This early detachment from the build platform for 19, 29 and 42 parameter specimens were already noted while printing by visual inspection. This could have been fixed by reheating the first few layers multiple times which could have resulted in better attachment of the low and mid VED (parameter 19 and 29 and 42) specimens to the build platform. However, the same build also had high VED

parameter 60 specimens getting printed which would have experienced excessive over melting to those specimens. Therefore, we decided to abort printing of those low and mid VED parameters specimens which by visual inspection were looked to be getting detached from the build platform. The learning from this attempt was to avoid printing many specimens with great variation in VEDs. Therefore, to continue, in the next attempt printing was repeated again but with only one set of parameter combination at a time which resulted in successful ten replicates for every combination without any build detachment issues.

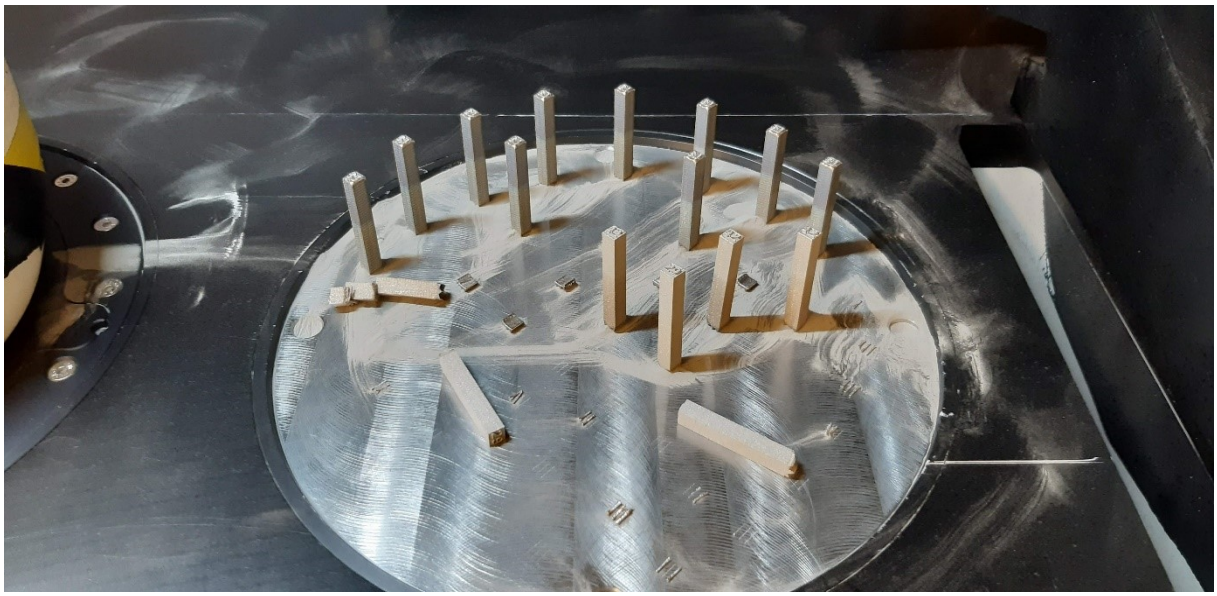

Picture 10 Vertical tensile test build. Picture: Tuomas Kantonen

4.4.2 Building compression test specimen

After successful tensile testing specimen printing, we attempted to print compression testing specimens. For compression testing we selected a 6 mm * 6 mm * 10 mm cuboidal geometry. Firstly, six pieces of each parameter combinations 19, 42 and 60 was attempted on the building platform. However, for this trial we have added a new support structure design which can be seen in Picture 11. Despite of smaller size and new support design, as can be seen from Picture 12 only five pieces of parameter combination 19 were successfully build while others had to be aborted because of bending off the building platform as observed visually during printing.

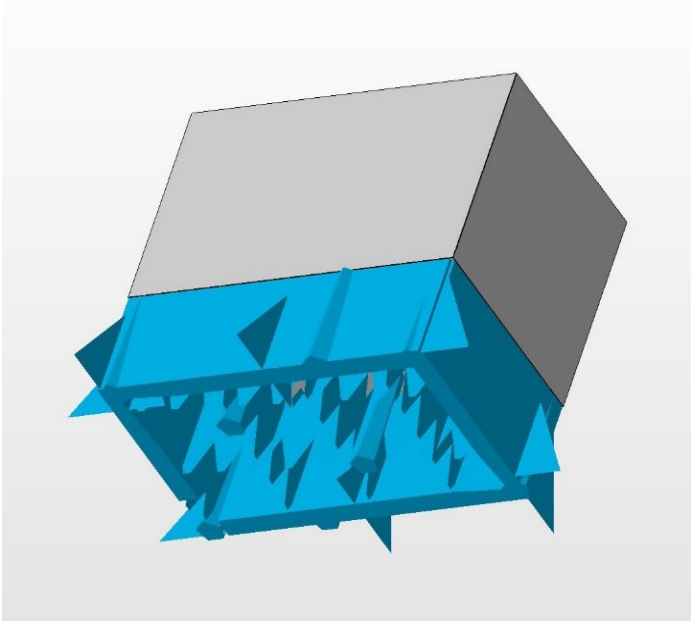

Picture 11 Support structure. Picture: Tuomas Kantonen

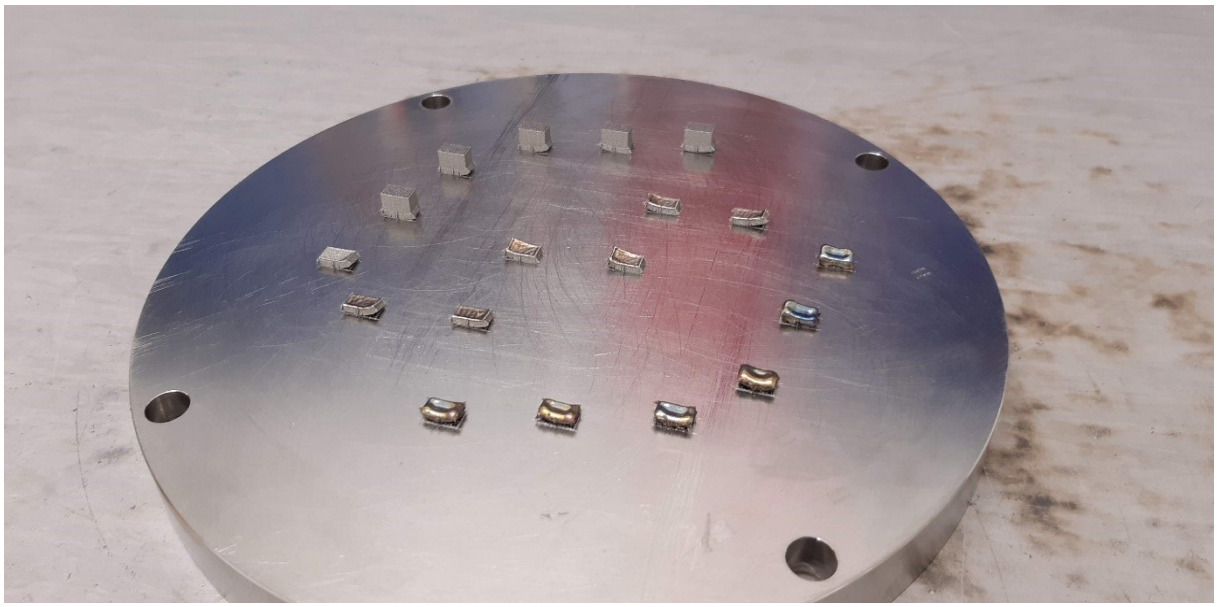

Picture 12 Compression test specimens. Picture: Tuomas Kantonen

The complete build was repeated again. During this trial though we have attempted to print the same size compression test specimens as previous attempt (6 mm * 6 mm * 10 mm) but with parameter combinations 29, 42 and 60 and the support structure was kept the same as in attempted during printing of small specimens in the very early attempts (see Picture 2). From this attempt all except one piece of parameter combination 29 were successfully produced (Picture 13, Picture 14 and Picture 15). The parameter combination 19 was left out from this build since we already had compression test specimen from previous build for that parameter combination.

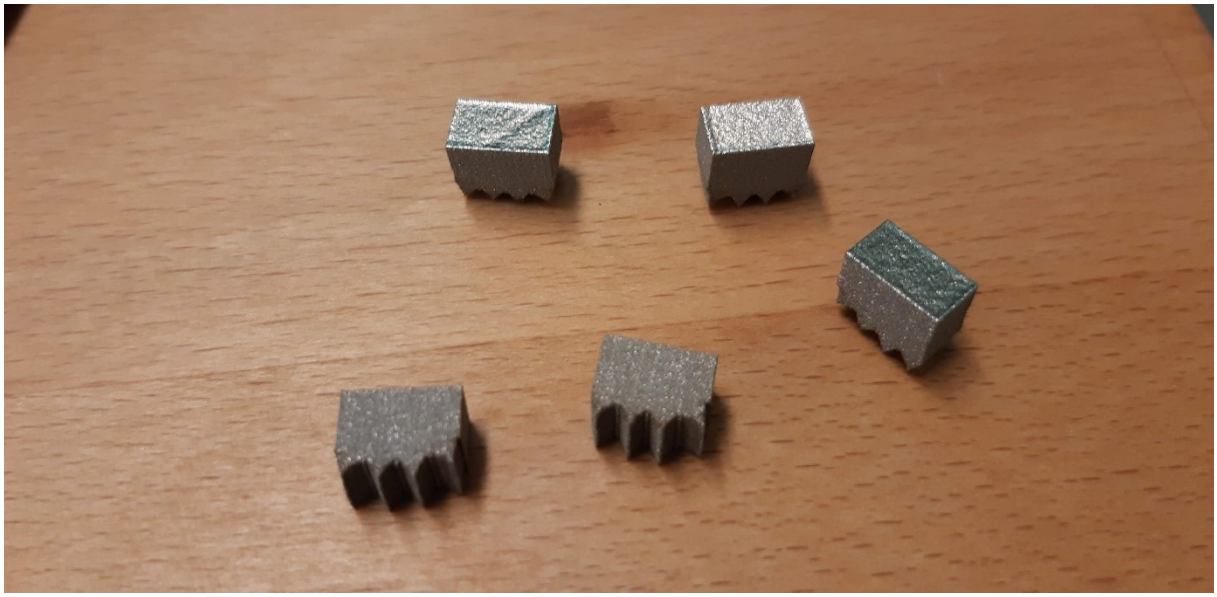

Picture 13 Compression test specimens 29. Picture: Tuomas Kantonen

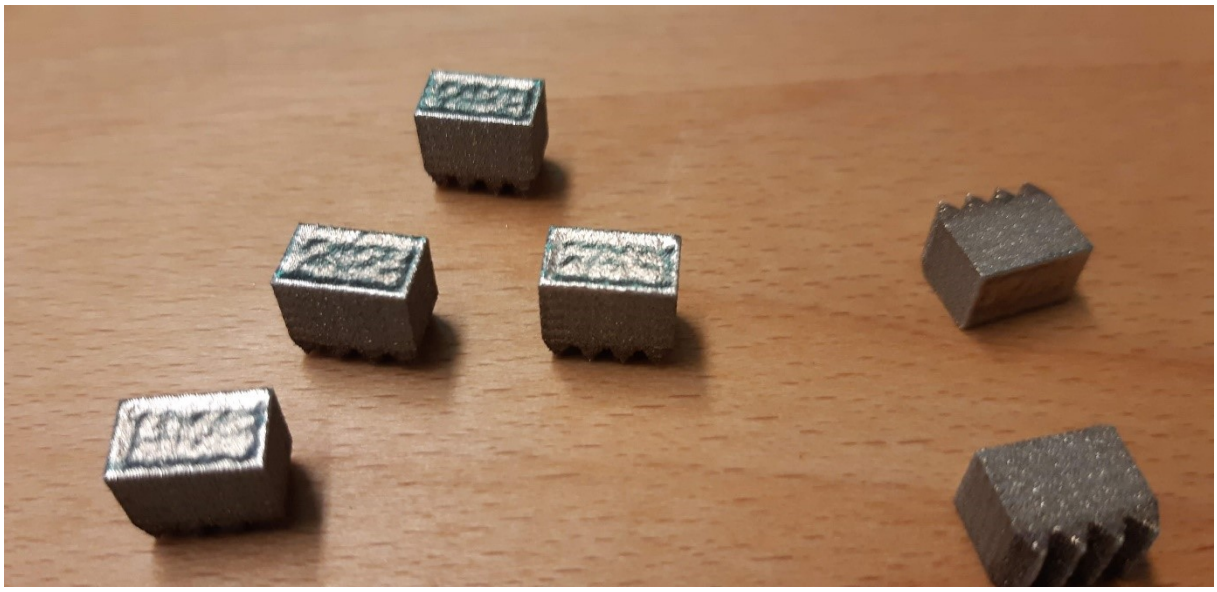

Picture 14 Compression test specimens 42. Picture: Tuomas Kantonen

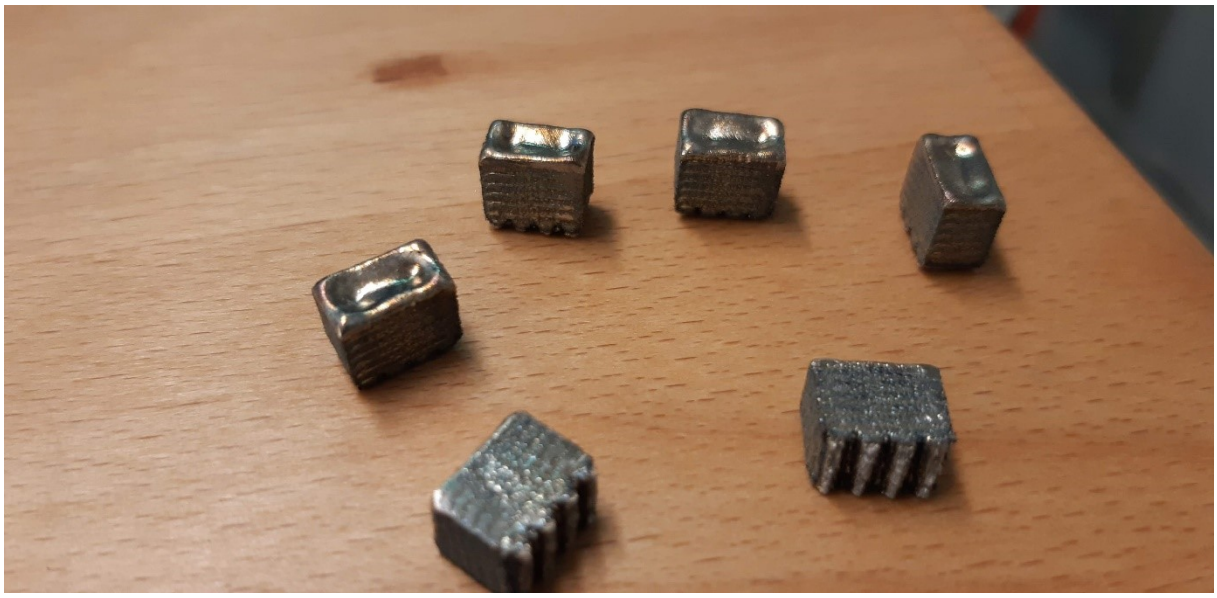

Picture 15 Compression test specimens 60. Picture: Tuomas Kantonen

4.4.3 Microstructure and phase compositions

Microstructures and phase compositions of specimens from parameters (19, 29, 42 and 60) were examined in as built conditions and after heat treatments. It is important to point out that finding an optimal heat treatment was out of the scope of this thesis and therefore the results did not include any further details about heat treatment optimization work. Electron backscatter diffraction (EBSD) maps in Picture 16 and Picture 17 show results of microstructure on the left and the phase composition on the right of all the four VED parameters in as-build condition. In the phase composition images on the right green represents ferritic and red austenitic phase. As it can be seen from the EBSD images that, in as built condition, the phase is mostly ferritic in all the samples. It is important to point out that the powder is also totally ferritic as per the supplier and also as verified by XRD results (not shown in this work).

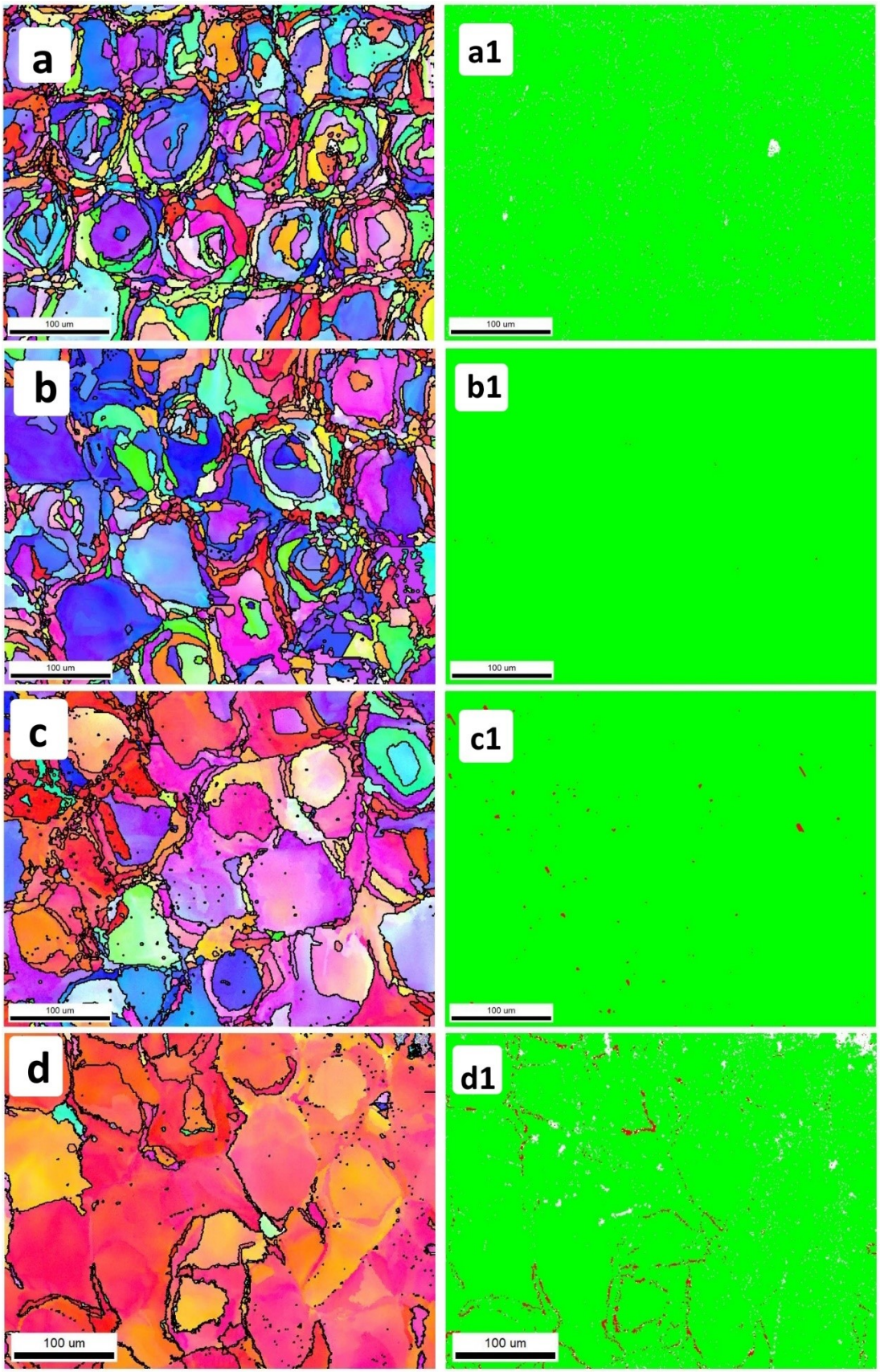

Picture 16: EBSD analysis of as built specimens showing grains (left) and phase (right) maps for (a & a1) Specimen 19, (b & b-1) Specimen 29, (c & c-1) Specimen 29 and (d & d1) Specimen 42, respectively. Picture: Jan Čapek

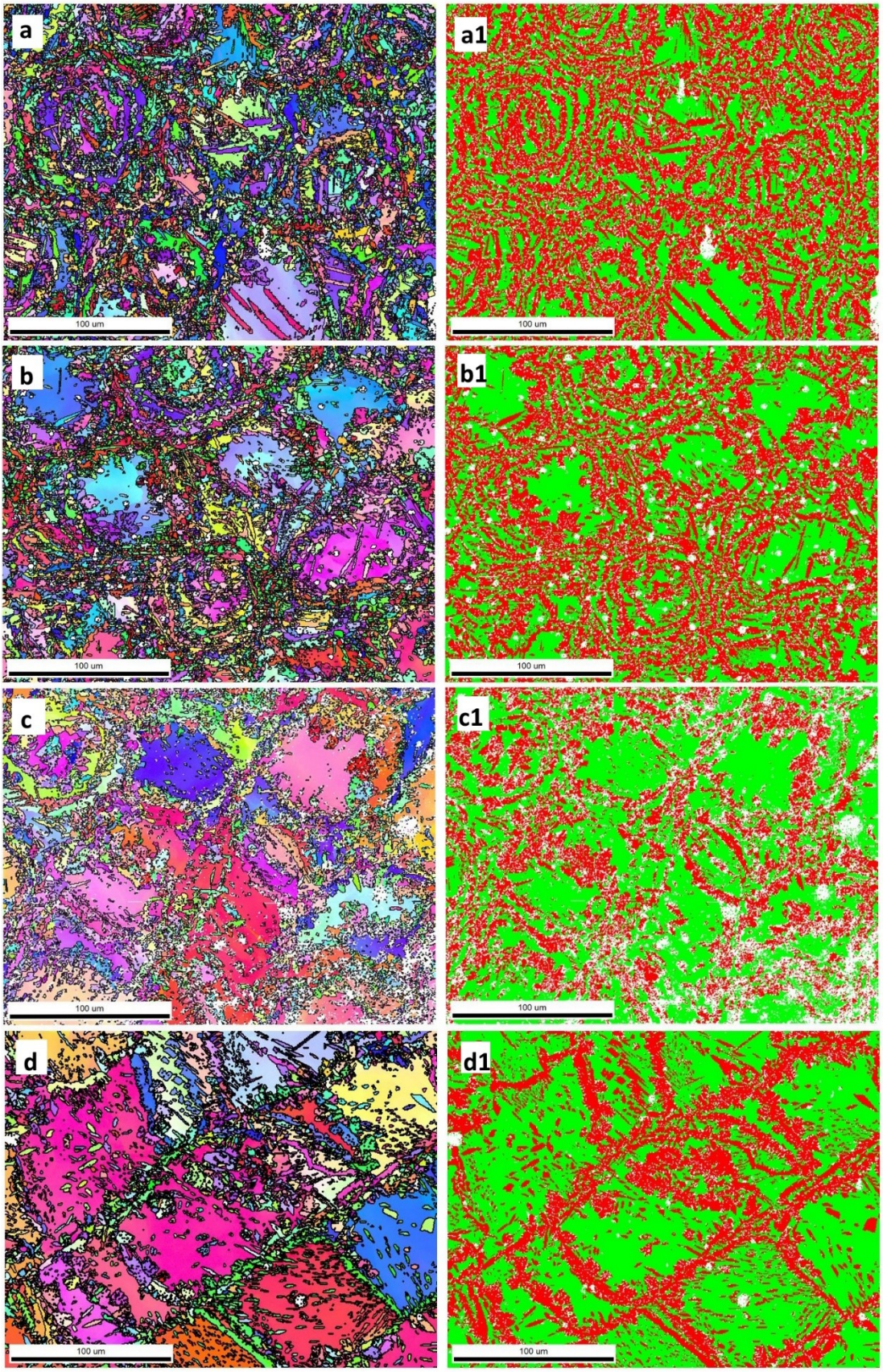

Picture 17: EBSD analysis of heat treated specimen at 900°C for 0.5 hours, showing grains (left) and phase (right) maps for (a & a1) Specimen 19, (b & b-1) Specimen 29, (c & c-1) Specimen 29 and (d & d1) Specimen 42, respectively. Picture: Jan Čapek

Only some austenitic regions can be seen in as built examined specimens between large ferritic grains as seen in Picture 16c1 and Picture 16d1. Also, it seems there is clearly an increasing trend in austenitic phase content in higher VED specimens as compared to low VED specimens in the as built state. Although not in the scope of this thesis our quick heat treatment results demonstrated that the austenitic phase (FCC) content can be increased significantly. For instance, annealing of all the specimens at 900 °C for 30 minutes showed increase in austenitic phase to 57.5% for parameter 19 (see Picture 17a1), 52% for parameter 29 (see Picture 17b1), 39% for parameter 42 (see Picture 17c1) and 41% for parameter 60 (see Picture 17d1).

5 Discussion

The first building attempt suffered from moving loose specimens because of the poor attachment to the building platform. This was most likely due to low energy density and unheated building platform resulting delamination between the build platform and the first layers as Gibson et al. suggests (2021). The result of the second building attempt is similar but since the lowest VED specimens were left out there were no loose specimens to ruin the build.

As mentioned, in the third build attempt, the lowest VED specimens were built straight on the platform without any support structure. Clearly there were macroscopic cracks on lower VED specimens as seen in Picture 6 and Picture 7. These cracks appeared on regular intervals throughout the build height. In fact, they appeared on geometrically notched locations like edges of the specimens as well as between the build platform and the first layers of the specimen which was caused by accumulation of stresses as explained by Platl et al. (2022). Also, significant delamination is visible on specimen with parameter 14 as can be seen in Picture 7, which, as previously mentioned is extreme case of cracking when residual stress exceeds material's yield strength (Mukherjee, Zhang & DebRoy 2017). Platl et al. (2022) suggests preheating the building platform to decrease the stresses and reduce cracking as well as delamination. Mukherjee, Zhang & DebRoy (2017) suggests that material's tendency to warping and delamination is dependent on residual stress to yield strength ratio. They suggest that using thinner layers while printing can decrease the residual stresses. They also discuss about the heat input and doubling it could lower residual stresses. However, they also suggest that the increased heat input can also increase the thermal distortion in build specimens drastically.

Even though the porosity of the specimens were not directly examined in this study it can be seen from Table 3 that the highest VED specimen have lowest density of those measured. This implies that there was more porosity in the over melted highest VED specimens. As explained by Simson et al. (2017), high energy density causes evaporation of molten material, leading to pore formation. Also, as King et al. (2014) and Zhao et al. (2020) explained, keyhole instability appears under high laser power and low scanning speed resulting in high VED which causes pores to the final specimen. Boes, Röttger & Theisen (2020) suggests that even the inefficient inert gas flow might be a cause for pore formation in case the by-products are not removed by gas flow.

There were visible spatters during melting the specimens by parameter 60 as shown in Picture 18. The spatters may have impact on the final products mechanical properties as mentioned before (Liu et al. 2015, Wang et al. 2017). In addition, the laser is partially absorbed by fumes rising from interaction zone of laser and powder bed causing different energy to the melt pool that was intended as mentioned by Boes, Röttger & Theisen (2020) and Wang et al. (2017). The mechanical properties were not examined in this study but based on the preliminary analysis we expect lower mechanical performance of the highest VED specimens compared to middle VED specimens.

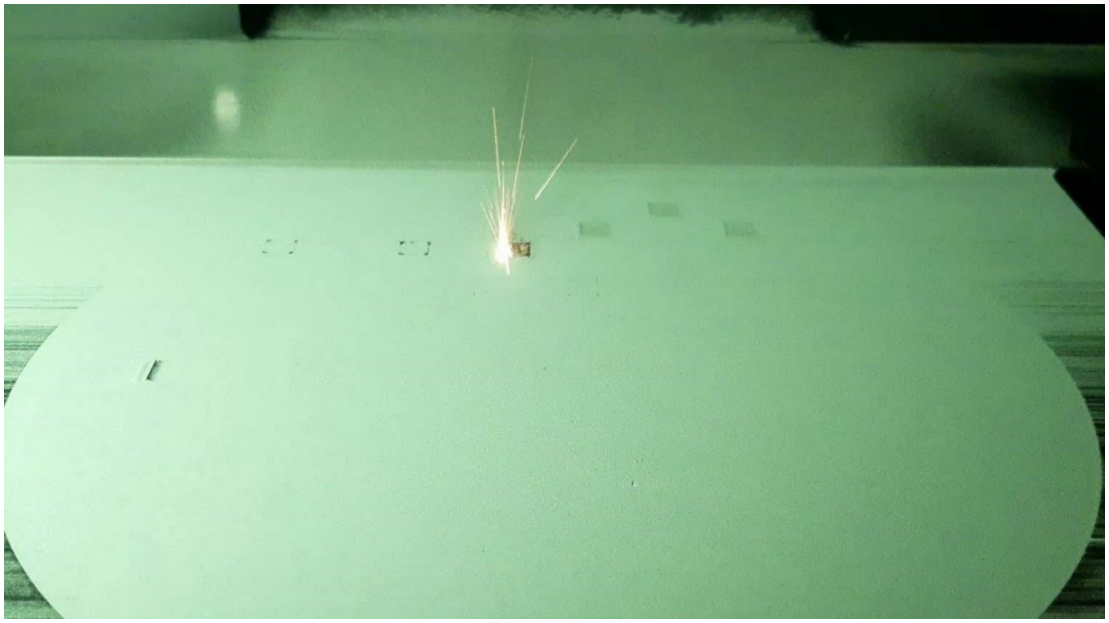

Picture 18 Spatters on high energy conditions. Picture: Tuomas Kantonen

The horizontal build attempt (Picture 9) of longer tensile test specimens clearly also suffered from delamination and because the process was going on during night the delaminated specimens were warped causing the powder recoater to hit them resulting to failed powder distribution to building platform. Since the heat expansion is related to length, the longer specimens lead to more expansion and therefore more stress in the specimen. The long specimens were delaminated and after cooling down warped forcefully as shown in Picture 9.

As previously mentioned, printing steels in L-PBF, the phase compositions can be affected with the variation in process parameters (Astafurov & Astafurova 2021). Since in this study the examined PANACEA powder was fully ferritic and the as built specimens were also primarily ferritic, there was no significant phase composition changes during the L-PBF processing. Although, in case of the highest VED specimen 60, there were traces of austenite phase and this specimen showed the highest presence of austenitic phase among all the four

examined specimens (Picture 16d1) in as-built state. However, it is worth pointing out that the austenite phase presence was still minimal, tiny deposits between large ferritic grains. Since austenitic steels have more desirable mechanical properties than ferritic, the heat treatments were done to see if austenitic phase can be increased. Although as mentioned earlier, optimization of heat treatment cycle is out of the scope of this thesis we have shown some preliminary results which shows increase in the austenitic phase. Although, significant increase of FCC (austenitic) phase was seen as previously mentioned but it was still far from getting a nearly fully austenitic specimen which would need further efforts in future to find optimal heat treatment parameters. However, the currently utilized heat treatment strategy did result in nearly 50%-50% of austenite-ferrite distribution which is commonly found in so called the dual-phase steels.

6 Conclusions

The purpose of the study was to find parameters to produce dense and deformation free novel Nickle free stainless steels specimens by L-PBF. The L-PBF machine used in this study was Aconity3d MIDI+ and powder used was commercially available stainless steel PANACEA from Sandvik AB. There were 60 different parameter combinations varying laser power, scanning speed and hatching distance. The building attempts with different geometries and support structures were made which gave result of four different parameter combinations for further building experiments. All four combinations gave dense and deformation free specimens when building specimens with several dimensions (length * width * height) such as (5 mm * 5 mm * 10 mm), (5 mm * 5 mm * 5 mm) and (10 mm * 10 mm * 5 mm). From those, further building experiments resulted in defect and deformation free specimens with dimensions such as (6.5 mm * 6.5 mm * 42 mm) and (6 mm * 6 mm * 10 mm) for further tensile and compression strength experiments, respectively. From the EBSD analysis it was shown that the original ferritic phase of the PANACEA powder was predominately retained in as-built printed specimens under all the four optimized processing conditions. The thesis also demonstrated that with a proper post thermal treatment strategy, fully ferritic PANACEA printed L-PBF specimens can be tailored for their phase content to nearly 50%-50% austenitic-ferritic dual phase steels.

In future, this work can be continued in several dimensions. Firstly, the printed PANACEA specimens should be evaluated for their mechanical properties such as tensile and compression as well fatigue behaviour. Moreover, further investigations on the parameter combinations as well as different types of support structures and heat treatment strategies to tailor microstructure should be studied. The four parameter combinations chosen in the study were not optimized for microstructure and mechanical properties but only for dense and deformation free specimens. Since the material is nickel free stainless steel and the assumed applications would be in health technology there should also be studies on corrosion and bio-tribology as well as biocompatibility characteristics of the printed specimens. Also, studying the powder with different L-PBF machines might be beneficial. The austenitic phase is more desired because of its superior mechanical properties so studying different heat treatments to achieve more austenitic phase would also be beneficial.

References

Aconity3d. 2022. Aconity3d homepage. www.aconity3d.com

Akilan, A. A., Nath, S. D., Enneti, R. K., Gupta, G., & Atre, S. V. 2022. Mechanical and corrosion properties of gas and water atomized laser-powder bed fusion fabricated 25Cr7Ni stainless steel. Manufacturing Letters, 31, 60-63.

Arabi-Hashemi, A., Maeder, X., Figi, R., Schreiner, C., Griffiths, S., & Leinenbach, C. 2020. 3D magnetic patterning in additive manufacturing via site-specific in-situ alloy modification. Applied Materials Today, 18, 100512.

Astafurov, S., & Astafurova, E. 2021. Phase composition of austenitic stainless steels in additive manufacturing: A review. Metals, 11(7), 1052.

Bai, S., Perevoshchikova, N., Sha, Y., & Wu, X. 2019. The effects of selective laser melting process parameters on relative density of the AlSi10Mg parts and suitable procedures of the archimedes method. Applied Sciences, 9(3), 583.

Bertoli, U. S., Wolfer, A. J., Matthews, M. J., Delplanque, J. P. R., & Schoenung, J. M. 2017. On the limitations of volumetric energy density as a design parameter for selective laser melting. Materials & Design, 113, 331-340.

Boes, J., Röttger, A., & Theisen, W. 2020. Microstructure and properties of high-strength C+ N austenitic stainless steel processed by laser powder bed fusion. Additive Manufacturing, 32, 101081.

Čapek, J., Polatidis, E., Casati, N., Pederson, R., Lyphout, C., & Strobl, M. 2022. Influence of laser powder bed fusion scanning pattern on residual stress and microstructure of alloy 718. Materials & design, 221, 110983.

Colosimo, B. M., & Grasso, M. 2020. In-situ monitoring in L-PBF: Opportunities and challenges. Procedia CIRP, 94, 388-391.

Cui, C., Uhlenwinkel, V., Schulz, A., & Zoch, H. W. 2019. Austenitic stainless steel powders with increased nitrogen content for laser additive manufacturing. Metals, 10(1), 61.

Davis, J. R. (Ed.). 1994. Stainless steels. ASM international.

DebRoy, T., Wei, H. L., Zuback, J. S., Mukherjee, T., Elmer, J. W., Milewski, J. O., Beese, A.M., Wilson-Heid, A., De, A., & Zhang, W. 2018. Additive manufacturing of metallic components–process, structure and properties. Progress in Materials Science, 92, 112-224.

du Plessis, A. 2019. Effects of process parameters on porosity in laser powder bed fusion revealed by X-ray tomography. Additive Manufacturing, 30, 100871.

Freitas, B. J. M., Rodrigues, L. C. M., Claros, C. A. E., Botta, W. J., Koga, G. Y., & Bolfarini, C. 2022. Ferritic-induced high-alloyed stainless steel produced by laser powder bed fusion (L-PBF) of 2205 duplex stainless steel: Role of microstructure, corrosion, and wear resistance. Journal of Alloys and Compounds, 918, 165576.

Gavriljuk, V. G., & Berns, H. 1999. High nitrogen steels: structure, properties, manufacture, applications. Springer Science & Business Media.

Gibson, I., Rosen, D. W., Stucker, B., Khorasani, M., Rosen, D., Stucker, B., & Khorasani, M. 2021. Additive manufacturing technologies (Vol. 17). Cham, Switzerland: Springer.

Großwendt, F., Röttger, A., Strauch, A., Chehreh, A., Uhlenwinkel, V., Fechte-Heinen, R., Walther, F., Weber, S., & Theisen, W. 2021. Additive manufacturing of a carbon-martensitic hot-work tool steel using a powder mixture–Microstructure, post-processing, mechanical properties. Materials Science and Engineering: A, 827, 142038.

Gu, D. 2015. Laser additive manufacturing of high-performance materials. Springer.

Karimi, M. S., Yeganeh, M., Zaree, S. A., & Eskandari, M. 2021. Corrosion behavior of 316L stainless steel manufactured by laser powder bed fusion (L-PBF) in an alkaline solution. Optics & Laser Technology, 138, 106918.

King, W. E., Barth, H. D., Castillo, V. M., Gallegos, G. F., Gibbs, J. W., Hahn, D. E., Kamath, C. & Rubenchik, A. M. 2014. Observation of keyhole-mode laser melting in laser powder-bed fusion additive manufacturing. Journal of Materials Processing Technology, 214(12), 2915-2925.

Li, N., Wang, T., Zhang, L., & Zhang, L. 2023. Crack initiation mechanism of laser powder bed fusion additive manufactured Al-Zn-Mg-Cu alloy. Materials Characterization, 195, 112415.

Li, R., Liu, J., Shi, Y., Wang, L., & Jiang, W. 2012. Balling behavior of stainless steel and nickel powder during selective laser melting process. The International Journal of Advanced Manufacturing Technology, 59(9), 1025-1035.

Liu, Y., Yang, Y., Mai, S., Wang, D., & Song, C. 2015. Investigation into spatter behavior during selective laser melting of AISI 316L stainless steel powder. Materials & Design, 87, 797-806.

Menzel J., Kirschner W. & Stein G. 1996. ISIJ International, 36, 893-900.

Mercelis, P., & Kruth, J. P. 2006. Residual stresses in selective laser sintering and selective laser melting. Rapid prototyping journal.

Merot, P., Morel, F., Pessard, E., Mayorga, L. G., Buttin, P., & Baffie, T. 2022. Fatigue strength and life assessment of L-PBF 316L stainless steel showing process and corrosion related defects. Engineering Fracture Mechanics, 276, 108883.

Moshiri, M., Candeo, S., Carmignato, S., Mohanty, S., & Tosello, G. 2019. Benchmarking of laser powder bed fusion machines. Journal of Manufacturing and Materials Processing, 3(4), 85.

Mukherjee, T., Zhang, W., & DebRoy, T. 2017. An improved prediction of residual stresses and distortion in additive manufacturing. Computational Materials Science, 126, 360-372.

Narasimharaju, S. R., Zeng, W., See, T. L., Zhu, Z., Scott, P., Jiang, X., & Lou, S. 2022. A comprehensive review on laser powder bed fusion of steels: Processing, microstructure, defects and control methods, mechanical properties, current challenges and future trends. Journal of Manufacturing Processes, 75, 375-414.

Platl, J., Rainer, D., Leitner, H., Turk, C., Galbusera, F., Demir, A. G., Previtali, B., & Schnitzer, R. 2022. Potential Causes for Cracking of a Laser Powder Bed Fused Carbon-free FeCoMo Alloy. BHM Berg-und Hüttenmännische Monatshefte, 1-7.

Reijonen, J., Revuelta, A., Riipinen, T., Ruusuvuori, K., & Puukko, P. 2020. On the effect of shielding gas flow on porosity and melt pool geometry in laser powder bed fusion additive manufacturing. Additive Manufacturing, 32, 101030.

Rombouts, M., Kruth, J. P., Froyen, L., & Mercelis, P. (2006). Fundamentals of selective laser melting of alloyed steel powders. CIRP annals, 55(1), 187-192.

Sames, W. J., List, F. A., Pannala, S., Dehoff, R. R., & Babu, S. S. (2016). The metallurgy and processing science of metal additive manufacturing. International materials reviews, 61(5), 315-360.

Simson, T., Emmel, A., Dwars, A., & Böhm, J. 2017. Residual stress measurements on AISI 316L samples manufactured by selective laser melting. Additive Manufacturing, 17, 183-189.

Sofras, C., Čapek, J., Arabi-Hashemi, A., Leinenbach, C., Frost, M., An, K., Logé, R.E., Strobl, M., & Polatidis, E. 2022. Tailored deformation behavior of 304L stainless steel through control of the crystallographic texture with laser-powder bed fusion. Materials & Design, 219, 110789.

Speidel, M. O., Magdowski, R., & Uggewitzer, P. J. 1996. Nickel-free austenitic stainless steels of exceptional strength and corrosion resistance. In CORROSION 96. OnePetro.

Stein G. & Hucklenbroich I. 2004. Manufacturing and Applications of High Nitrogen Steels, Materials and Manufacturing Processes, 19:1, 7-17.

Tang, M., Pistorius, P. C., & Beuth, J. L. 2017. Prediction of lack-of-fusion porosity for powder bed fusion. Additive Manufacturing, 14, 39-48.

Uddin, M. J., Siller, H. R., Mirshams, R. A., Byers, T. A., & Rout, B. 2022. Effects of proton irradiation on nanoindentation strain-rate sensitivity and microstructural properties in L-PBF 17–4 PH stainless steels. Materials Science and Engineering: A, 837, 142719.

Wang, D., Wu, S., Fu, F., Mai, S., Yang, Y., Liu, Y., & Song, C. 2017. Mechanisms and characteristics of spatter generation in SLM processing and its effect on the properties. Materials & Design, 117, 121-130.

Yang, G., Xie, Y., Zhao, S., Qin, L., Wang, X., & Wu, B. 2022. Quality control: Internal defects formation mechanism of selective laser melting based on laser-powder-melt pool interaction: A review. Chinese Journal of Mechanical Engineering: Additive Manufacturing Frontiers, 100037.

Yang, K. & Ren, Y. 2010. Nickel-free austenitic stainless steels for medical applications. Science and Technology Advanced Materials, 11:2010, 1-13.

Zhao, C., Parab, N. D., Li, X., Fezzaa, K., Tan, W., Rollett, A. D., & Sun, T. 2020. Critical instability at moving keyhole tip generates porosity in laser melting. Science, 370(6520), 1080-1086.

Appendices

Appendix 1 List of different LPBF parameter combinations

Table 4 Reference LPBF processing parameters

	Reference from Arabi-Hashemi et al.	Reference from Aconity's guide for AISI 316L
P	200	150
v	800	800
h	0,125	0,08
d	0,03	0,03
VED	66,7	78,1

Table 5 LPBF processing parameters used in this study across run numbers 1 to 60.

Run	1	2	3	4	5	6	7	8	9	10	11	12	13	14	15
P	140	120	160	140	180	110	200	160	120	110	225	180	140	120	250
v	2000	1600	2000	1600	2000	1200	2000	1600	1200	1000	2000	1600	1200	1000	2000
h	0,05	0,05	0,05	0,05	0,05	0,05	0,05	0,05	0,05	0,05	0,05	0,05	0,05	0,08	0,08
d	0,03	0,03	0,03	0,03	0,03	0,03	0,03	0,03	0,03	0,03	0,03	0,03	0,03	0,03	0,03
VED	46,7	50,0	53,3	58,3	60,0	61,1	66,7	66,7	66,7	73,3	75,0	75,0	77,8	50,0	52,1
	16	17	18	19	20	21	22	23	24	25	26	27	28	29	30
P	200	160	110	140	225	300	180	120	250	160	200	140	180	110	300
v	1600	1200	800	1000	1600	2000	1200	800	1600	1000	1200	800	1000	600	1600
h	0,08	0,08	0,08	0,08	0,08	0,08	0,08	0,08	0,08	0,08	0,08	0,08	0,08	0,08	0,08
d	0,03	0,03	0,03	0,03	0,03	0,03	0,03	0,03	0,03	0,03	0,03	0,03	0,03	0,03	0,03
VED	52,1	55,6	57,3	58,3	58,6	62,5	62,5	62,5	65,1	66,7	69,4	72,9	75,0	76,4	78,1
	31	32	33	34	35	36	37	38	39	40	41	42	43	44	45
P	225	200	150	120	250	225	180	140	300	250	200	160	110	225	300
v	1200	1000	800	600	1200	1000	800	600	1200	1000	800	600	400	800	1000

h	0,08	0,08	0,08	0,08	0,08	0,08	0,08	0,08	0,08	0,08	0,08	0,08	0,08	0,08	0,08
d	0,03	0,03	0,03	0,03	0,03	0,03	0,03	0,03	0,03	0,03	0,03	0,03	0,03	0,03	0,03
VED	78,1	83,3	78,1	83,3	86,8	93,8	93,8	97,2	104,2	104,2	104,2	111,1	114,6	117,2	125,0

	46	47	48	49	50	51	52	53	54	55	56	57	58	59	60
P	180	120	250	200	140	300	225	160	250	180	300	200	225	250	300
v	600	400	800	600	400	800	600	400	600	400	600	400	400	400	400
h	0,08	0,08	0,08	0,08	0,08	0,08	0,08	0,08	0,08	0,08	0,08	0,08	0,08	0,08	0,08
d	0,03	0,03	0,03	0,03	0,03	0,03	0,03	0,03	0,03	0,03	0,03	0,03	0,03	0,03	0,03
VED	125,0	125,0	130,2	138,9	145,8	156,3	156,3	166,7	173,6	187,5	208,3	208,3	234,4	260,4	312,5

Note: The notations p, v, h, d, and VED represent power, scanning velocity, hatch distance, layer thickness, and volume energy density, respectively.